J. Fluid Mech. (1993), *vol.* 250, *pp.* 339–369

Particle-driven gravity currents

By ROGER T. BONNECAZE†, HERBERT E. HUPPERT AND JOHN R. LISTER

Institute of Theoretical Geophysics, Department of Applied Mathematics and Theoretical Physics, University of Cambridge, Silver Street, Cambridge CB3 9EW, UK

(Received 28 May 1992)

Gravity currents created by the release of a fixed volume of a suspension into a lighter ambient fluid are studied theoretically and experimentally. The greater density of the current and the buoyancy force driving its motion arise primarily from dense particles suspended in the interstitial fluid of the current. The dynamics of the current are assumed to be dominated by a balance between inertial and buoyancy forces; viscous forces are assumed negligible. The currents considered are two-dimensional and flow over a rigid horizontal surface. The flow is modelled by either the single- or the two-layer shallow-water equations, the two-layer equations being necessary to include the effects of the overlying fluid, which are important when the depth of the current is comparable to the depth of the overlying fluid. Because the local density of the gravity current depends on the concentration of particles, the buoyancy contribution to the momentum balance depends on the variation of the particle concentration. A transport equation for the particle concentration is derived by assuming that the particles are vertically well-mixed by the turbulence in the current, are advected by the mean flow and settle out through the viscous sublayer at the bottom of the current. The boundary condition at the moving front of the current relates the velocity and the pressure head at that point. The resulting equations are solved numerically, which reveals that two types of shock can occur in the current. In the late stages of all particle-driven gravity currents, an internal bore develops that separates a particle-free jet-like flow in the rear from a dense gravity-current flow near the front. The second type of bore occurs if the initial height of the current is comparable to the depth of the ambient fluid. This bore develops during the early lock-exchange flow between the two fluids and strongly changes the structure of the current and its transport of particles from those of a current in very deep surroundings. To test the theory, several experiments were performed to measure the length of particle-driven gravity currents as a function of time and their deposition patterns for a variety of particle sizes and initial masses of sediment. The comparison between the theoretical predictions, which have no adjustable parameters, and the experimental results are very good.

1. Introduction

A gravity current is a wedge of fluid intruding laterally into an ambient body of fluid of a different density, as depicted for example in figure 1, which shows a gravity current propagating along a horizontal surface below the ambient fluid. The buoyancy or gravitational force driving the motion may be due to differences in composition or temperature between the gravity current and the ambient fluid, or the two fluids may

† Current address: Department of Chemical Engineering, The University of Texas at Austin, Austin, Texas, 78712-1062, USA.

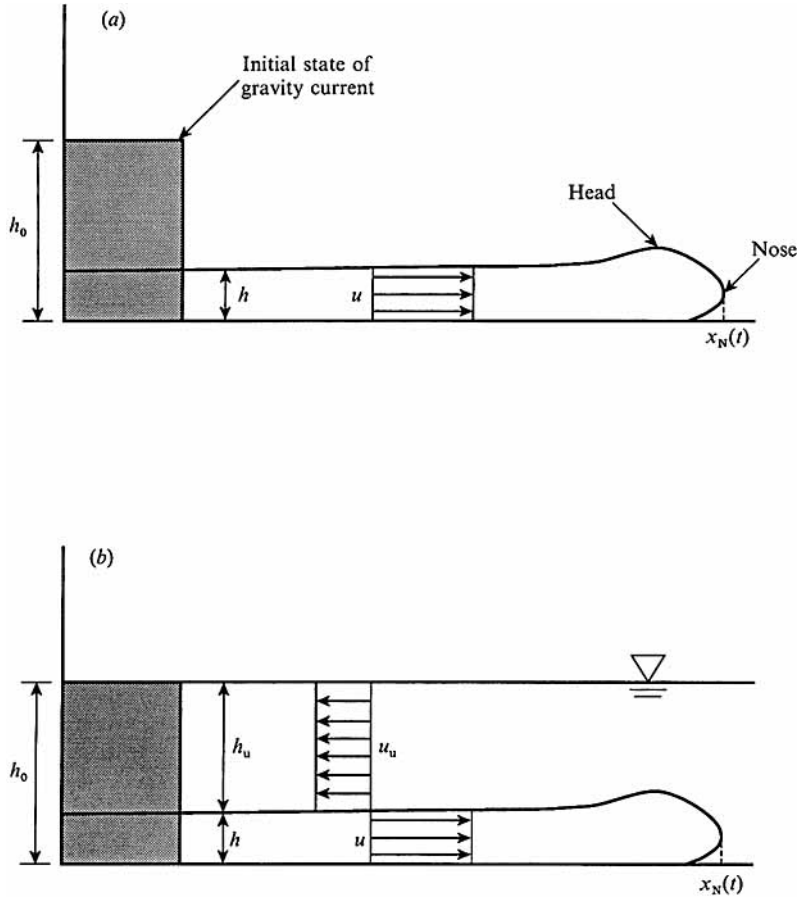

FIGURE 1. Schematic representation of a dense gravity current intruding into a less dense body of ambient fluid that is: (*a*) very deep compared to the depth of the current; (*b*) of comparable depth to the current.

even be physically different liquids. A density difference can also arise from the suspension of particles in the fluid forming the current. The bulk density of such a suspension may be greater than its surroundings, resulting in a gravity current. We term this a particle-driven gravity current since the presence of the particles is the cause of the motion.

Particle-driven gravity currents are considerably more complex than homogeneous currents because the particle concentration, and hence the driving buoyancy force, change with time and position along the current. Particles may settle out, which reduces the density difference. Alternatively, if the current is passing sufficiently rapidly over an erodible bed, sediment may be entrained, which increases the particle concentration and driving buoyancy force. Both the settling and entrainment rates depend on the velocity and dimensions of the gravity current, and so there is a strong coupling between the sediment transport and the dynamics of the flow.

Particle-driven gravity currents are important in many environmental and geological situations. In the form of industrial or estuarial effluents they are an important mechanism for transporting sediment that may have adsorbed pollutants. The erosive power of particle-driven gravity currents, often called turbidity currents in a geological context, is responsible for the formation of submarine canyons on continental shelves

and the transport of silt and sand into the deep oceans (Inman, Nordstrom & Flick 1976). Some turbidites (the sedimentary deposits of ancient turbidity currents) have become oil reservoirs (Perrodon 1985). A particle-driven gravity current with reversing buoyancy can occur when the interstitial fluid has a lesser density than the surroundings. For example, sediment-laden fresh water from a river outflow can actually sink in a salty bay or ocean outlet provided there are enough dense particles in suspension (Wright *et al.* 1990). When sufficient particles have settled, however, the bulk density of the gravity current will become less than that of the surroundings, and the gravity current will rise as a plume.

This work is motivated by a desire to understand and model such flows and the resulting sedimentary transport processes. In this paper we analyse the specific problem of a particle-driven gravity current of fixed volume spreading over a rigid horizontal surface. We assume that the current is two-dimensional, though the model can be easily extended to include an axisymmetric flow (Bonnecaze, Huppert & Lister 1993). Our analysis describes the settling of the particles and their advection within the current, but entrainment of sediment is not considered. The particles in the current are assumed to be dilute, non-cohesive and monodisperse with equal settling velocities. We also assume that the viscous forces acting on the current are negligible, except perhaps at its head, and that the force balance is dominated by inertia and buoyancy. This is often the case for many practical situations.

There has been a great deal of research on homogeneous gravity currents, and many of the concepts and results are useful for analysis of particle-driven currents. The dynamics of the front or nose of a gravity current intruding into a very deep body of fluid with negligible viscous forces acting on the current was analysed using the Bernoulli equation first by von Kármán (1940) and later correctly by Benjamin (1968). They both arrived at the result that the velocity at the front of the current u_N and the height or depth of the current just to the rear of the head h_N are related by $u_N = Fr(g'h_N)^{\frac{1}{2}}$, where the Froude number Fr is constant. In this relationship the reduced gravity g' is defined by $g' = (\rho_c - \rho_a)g/\rho_a$, where ρ_c and ρ_a are the densities of the current and the ambient fluid respectively, and g is the gravitational acceleration. Benjamin found that the value of the Froude number Fr depends on the ratio of the height of the head of the current to the depth of the ambient fluid and has a theoretical value of $\sqrt{2}$ for a current intruding into very deep surroundings.

A homogeneous gravity current dominated by inertial and buoyancy forces can be modelled by the shallow-water equations, which admit a long-time asymptotic similarity solution (Fannelop & Waldman 1972; Hoult 1972; Chen 1980). The length of a two-dimensional homogeneous gravity current, $x_N(t)$, is given by $x_N(t) = C(g'q)^{\frac{1}{3}}t^{\frac{2}{3}}$, where t is the time since release and q is the fixed volume per unit width of the current. The constant C depends on the value of Fr at the nose. The initial evolution of a lock-exchange flow, in which a fixed volume of dense fluid held behind a gate is instantaneously released into an ambient fluid, has been studied by Huppert & Simpson (1980). In this so-called slumping phase, which precedes the self-similar regime, they found experimentally that the length increased almost linearly with time. The approach to the similarity form was studied further by Rottman & Simpson (1983) with experiments and a model based on the shallow-water equations. An interesting observation of their work was the formation of an internal bore if the initial height of the gravity current behind the lock was more than 70% of the depth of the ambient fluid. Until this bore overtook the front, the height of the current at the front remained constant, resulting in a constant velocity at the nose, and hence the length of the current increased linearly with time.

Inertial forces do not dominate the dynamics of a gravity current indefinitely. When the current has reached a sufficient length the viscous forces acting on the bottom of the current along the rigid horizontal surface become more important than the inertial forces. The conditions for the transition from inertially to viscously dominated flow for a current of fixed volume has been determined experimentally by Huppert & Simpson (1980) and theoretically by Huppert (1982). The transition can be written in terms of the criterion $(u_N h_N/\nu)(h_N/x_N) \approx 2.25$, where the left-hand side is essentially a Reynolds number and ν is the kinematic viscosity of the current. As the current lengthens and the velocity and height at the nose decrease, the Reynolds number decreases below the critical value and viscous forces dominate the inertial forces. The dynamics of a gravity current dominated by a viscous–buoyancy balance have been analysed by Huppert (1982) using lubrication theory.

In §2.1 we incorporate some of the results from the inertial studies in order to construct a model for a particle-driven gravity current spreading over a horizontal rigid boundary in very deep ambient fluid. We use the single-layer shallow-water equations and a vertically averaged advective conservation equation, which includes settling, for the particle concentration. The model assumes that the dynamics of the current are dominated by a balance between inertial and buoyancy forces and that the particles are vertically well-mixed due to sufficiently vigorous turbulent mixing. The Froude-number condition is specified at the moving front of the gravity current, whose position must be determined as part of the problem. The height and velocity profiles from the similarity solutions for a fixed-volume homogeneous or non-settling gravity current are reviewed for later comparison with those for a particle-driven gravity current.

In some applications and in the early times of our experiments, however, the depth of the overlying fluid is comparable to that of the gravity current. In order to account for the effects of the overlying fluid, we describe in §2.2 a modification to our model that incorporates the two-layer shallow-water equations and the nose condition of Huppert & Simpson (1980). These changes lead to the prediction of the slumping phase and bore between the two layers. The inclusion of these phenomena is important for modelling gravity currents in shallow ambient fluids, such as in our experiments or for turbidity currents in shallow seas. We should point out that both the single-layer and two-layer models have no free parameters, because the nose condition and the settling velocity of the particles are determined either theoretically or from independent experiments.

Since the equations that describe particle-driven gravity currents do not admit analytic solutions, we outline a method for numerical solution of the model equations briefly in §3 and in more detail in Appendix A. We also present typical height, velocity and concentration profiles from the solution of the equations of fluid and particle transport and discuss their evolution. In particular, the structure of the current has an important effect on the settling of particles in the current, which in turn affects the dynamics of the current. In §4 we describe some lock-exchange experiments in which dense suspensions of particles were released into a long flume from behind a gate. We present data for the length of the gravity current as a function of time and for the final deposition patterns of the flow. These experimental results are then compared to the numerical predictions of the two-layer model. In §5 we summarize and discuss our results and conclude with an outline of future work on particle-driven gravity currents.

2. Theory

2.1. *Single-layer model*

Consider a particle-driven gravity current created by the release of a well-mixed suspension of bulk density ρ_c into a deep ambient body of fluid of lesser density ρ_a. The volume of the current is fixed and we assume that it flows over a rigid horizontal surface, as illustrated in figure 1(*a*). The flow is driven by the difference between the bulk density of the current and the density of the ambient fluid. The density of the current, which may vary along its length, is the local volume average of the particle density ρ_p and the interstitial fluid density ρ_i and is given by

$$\rho_c(\phi) = (\rho_p - \rho_i)\,\phi + \rho_i, \tag{1}$$

where ϕ is the volume fraction occupied by the particles.

The initial flow following the release of a gravity current of finite volume is usually a complex three-dimensional unsteady flow, but soon after release the current has spread sufficiently that its length is very much greater than its height, $h(x, t)$, which is slowly varying over the horizontal position x and in time t. For such conditions, it is reasonable to neglect vertical accelerations in the flow and to assume a hydrostatic pressure distribution. We also assume that the Reynolds number of the flow is sufficiently large that viscous forces are negligible and that the flow dynamics are dominated by a balance between buoyancy and inertial forces. We can then assume that the horizontal velocity field in the current $u(x, t)$ is vertically uniform. By extension of previous successful analyses of fixed-volume saline gravity currents, we neglect the effects of entrainment of ambient fluid (Huppert & Simpson 1980; Rottman & Simpson 1983), though the effects of entrainment are now being investigated (Hallworth *et al.* 1993).

These assumptions lead to the shallow-water equations, which describe conservation of mass,

$$\frac{\partial h}{\partial t} + \frac{\partial}{\partial x}(uh) = 0, \tag{2}$$

and conservation of momentum,

$$\frac{\partial}{\partial t}(uh) + \frac{\partial}{\partial x}[u^2 h + \tfrac{1}{2} g'(\phi)\, h^2] = 0, \tag{3}$$

where the reduced gravity $g'(\phi) = [\rho_c(\phi) - \rho_a]\, g/\rho_a$ is a function of the volume fraction of particles. We have assumed that ϕ is small and used a Boussinesq approximation which neglects terms $O(\phi)$ and smaller in the equations of mass and momentum conservation except for the gravitational terms. We have also assumed that the ambient fluid is very deep compared with the depth of the gravity current so that the effects of the overlying fluid on the dynamics of the current can be neglected.

The particle concentration varies throughout the current due to advection and settling. In this paper we neglect particle entrainment on the assumption that the current velocities are insufficient to lift deposited sediment into the current. We do consider the flow sufficiently vigorous, however, that turbulent mixing maintains a vertically uniform particle concentration in the current, without any detrainment of particle-free fluid at the top of the current. We assume that the particles leave the current only through the viscous sublayer at the base with a flux $-v_s \phi$, where v_s

denotes the settling velocity of an isolated particle that is appropriate when the particle concentration is small. This model has been used successfully in other studies of sedimentation from turbulent suspensions (Einstein 1968; McCave 1970; Martin & Nokes 1988, 1989).

We then derive the equation of particle conservation,

$$\frac{\partial}{\partial t}(\phi h)+\frac{\partial}{\partial x}(u\phi h) = -v_s\phi, \tag{4a}$$

which may be written in the perhaps more familiar alternative form,

$$\frac{\partial \phi}{\partial t}+u\frac{\partial \phi}{\partial x} = -v_s\frac{\phi}{h}, \tag{4b}$$

by use of (2). We note from the right-hand side of (4*b*) that the rate of decrease of the particle concentration increases with decreasing depth of the current.

The two boundary conditions for (2)–(4) are zero flow at the end wall $x = 0$,

$$u(0, t) = 0, \tag{5}$$

and the condition at the front of the current, which relates the velocity to the pressure head $g'(\phi)h$ at the nose $x = x_N(t)$,

$$u_N = Fr[g'(\phi_N)h_N]^{\frac{1}{2}}, \tag{6}$$

where Fr is the Froude number. For gravity currents intruding into a deep ambient fluid with no viscous dissipation, Benjamin (1968) showed theoretically that $Fr = \sqrt{2}$, while experimentally Huppert & Simpson (1980) found a value of 1.19.

The head of a current is actually a zone of rolling, billowing three-dimensional turbulent motion, and the Froude-number condition at the nose in (6) is an effective lumped boundary condition, which represents the loss of momentum from the current to the ambient fluid as it intrudes into the surroundings. Benjamin's theoretical value for Fr assumes that the momentum loss is due only to moving the ambient fluid out of the current's path. The experimental value of the Froude number is somewhat lower because of viscous drag and turbulent Reynolds stresses, which cause additional momentum transfer at the head and further retard the flow of the current.

It is convenient to non-dimensionalize (2)–(6) with some of the initial parameters of the current. We non-dimensionalize lengths, time and velocities by h_0, $(h_0/g_0')^{\frac{1}{2}}$ and $(g_0'h_0)^{\frac{1}{2}}$, where h_0 is the initial height of the gravity current, g_0' is the initial contribution of the particles $(\rho_p-\rho_i)\phi_0 g/\rho_a$ to the reduced gravity, and ϕ_0 is the initial volume fraction of particles. Further, the volume fraction of particles is rescaled by ϕ_0. Using the previous symbols to represent the now non-dimensional variables, the dimensionless equations are given by

$$\frac{\partial h}{\partial t}+\frac{\partial}{\partial x}(uh) = 0, \tag{7}$$

$$\frac{\partial}{\partial t}(uh)+\frac{\partial}{\partial x}[u^2h+\tfrac{1}{2}(\phi-\gamma)h^2] = 0, \tag{8}$$

$$\frac{\partial \phi}{\partial t}+u\frac{\partial \phi}{\partial x} = -\beta\frac{\phi}{h}, \tag{9}$$

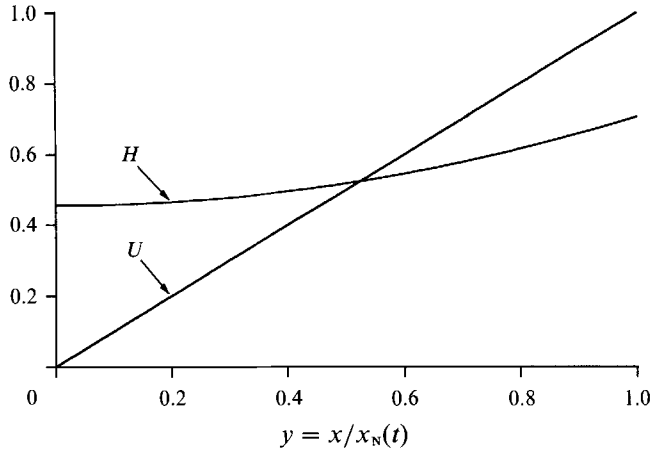

FIGURE 2. The long-time self-similar velocity $U(y)$ and height $H(y)$ for a homogeneous gravity current of fixed volume with $Fr = 1.19$ at the nose.

with the boundary conditions

$$u = 0 \quad (x = 0) \tag{10}$$

and

$$u = Fr[(\phi - \gamma)\, h]^{\frac{1}{2}} \quad [x = x_N(t)]. \tag{11}$$

The parameter $\gamma = (\rho_a - \rho_i)/[(\rho_p - \rho_i)\,\phi_0]$ is the contribution of the interstitial fluid to the reduced gravity. The settling number $\beta = v_s/(g_0' h_0)^{\frac{1}{2}}$ is a non-dimensional settling velocity. In this paper we will only consider cases in which the densities of the interstitial and ambient fluid are equal, so that $\gamma = 0$. Sparks *et al.* (1992), however, have examined the problem of particle-driven gravity currents with reversing buoyancy, for which $\gamma > 0$.

When $\beta = 0$ and there is no settling, (7)–(11) possess a long-time similarity solution (Fannelop & Waldman 1972; Hoult 1972; Chen 1980)

$$h(x, t) = \dot{x}_N^2(t)\, H(y), \tag{12}$$

$$u(x, t) = \dot{x}_N(t)\, U(y), \tag{13}$$

where

$$H(y) = \tfrac{1}{4}(y^2 - 1) + \frac{1}{Fr^2}, \tag{14}$$

$$U(y) = y, \tag{15}$$

$$x_N(t) = [27 Fr^2 x_0/(12 - 2Fr^2)]^{\frac{1}{3}}\, t^{\frac{2}{3}}, \tag{16}$$

and the similarity variable y is defined by $y = x/x_N(t)$. The initial volume of the gravity current x_0 in (16) is non-dimensionalized by h_0^2. Self-similar solutions also exist for homogeneous gravity currents in which the volume of the current increases proportional to t^α, where α is a non-negative constant, but there are some restrictions on their existence, as discussed by Grundy & Rottman (1985).

Figure 2 shows the self-similar velocity and height profiles of a homogeneous or non-settling gravity current for $Fr = 1.19$. The abrupt changes in the velocity and height at the nose are a consequence of the nose condition in (6). The velocity increases linearly from zero at the tail to the nose velocity at the head, and the height of the current

increases quadratically from the tail to the head. The variation of the height of the current creates an adverse pressure gradient, which decelerates the flow. This loss of momentum throughout the current may be attributed to the nose condition, which represents a sink of momentum. As we shall see, when particles settle out the uneven loss of sediment in the current prevents this balance from being maintained and a shock develops.

Initially, we tried to match our experimental data for particle-driven gravity currents with the numerical solution of (7)–(11) for $\beta \neq 0$. This was not successful, and we concluded that, since our experiments were performed in a shallow ambient layer and the depth of this layer was comparable to the gravity-current depth, we must include the effects of the overlying fluid. While this increases the complexity of the model somewhat, it does not change the fundamental hydraulic and particle-transport assumptions. Indeed, since the two-layer model describes the experiments well, we expect the single-layer model to be applicable for particle-driven gravity currents intruding into deep surroundings. In the next section we outline the two-layer shallow-water equations and the new nose condition, which account for the overlying fluid in our experiments.

2.2. *Two-layer fluid model*

When a gravity current intrudes into a relatively shallow surrounding fluid, the dynamics of the overlying fluid must be considered as well as those of the current. Huppert & Simpson (1980) observed experimentally that if the depth of the gravity current is greater than 10% of the depth of the ambient fluid, the Froude number at the nose depends on the ratio of these depths and is less than the value of the Froude number in deep surroundings. In addition, when a fixed volume of fluid is released from behind a gate in a lock-exchange-type experiment, Rottman & Simpson (1983) observed that when the overlying fluid replacing the slumping gravity current reached the endwall, a bore developed and propagated towards the head of the current. These effects result in the initial slumping behaviour of a gravity current of fixed volume in which the length increases linearly with time. The incorporation of the mass and momentum balance for the ambient fluid and slightly modified boundary conditions captures both the bore and the slumping behaviour, which affect the particle transport and long-time behaviour of a particle-driven current.

Consider a particle-driven gravity current created by the release of a suspension into a body of fluid with a fixed total depth of h_0, as illustrated in figure 1 (*b*). Using the same hydraulic assumptions as in the single-layer model, we can derive the dimensionless equations of mass conservation for the two layers as

$$\frac{\partial h}{\partial t}+\frac{\partial}{\partial x}(uh) = 0, \tag{17}$$

$$\frac{\partial h_{\mathrm{u}}}{\partial t}+\frac{\partial}{\partial x}(u_{\mathrm{u}} h_{\mathrm{u}}) = 0, \tag{18}$$

and the dimensionless momentum balance for the two layers as

$$\frac{\partial}{\partial t}(uh)+\frac{\partial}{\partial x}(u^2h+\tfrac{1}{2}\phi h^2)+h\frac{\partial p}{\partial x} = 0, \tag{19}$$

$$\frac{\partial}{\partial t}(u_{\mathrm{u}} h_{\mathrm{u}})+\frac{\partial}{\partial x}(u_{\mathrm{u}}^2 h_{\mathrm{u}})-\gamma h_{\mathrm{u}}\frac{\partial h}{\partial x}+h_{\mathrm{u}}\frac{\partial p}{\partial x} = 0, \tag{20}$$

while the equation of particle conservation is again

$$\frac{\partial \phi}{\partial t}+u\frac{\partial \phi}{\partial x}=-\beta\frac{\phi}{h}, \tag{21}$$

where h_u and u_u are the depth and velocity of the upper or overlying ambient fluid, and p is the pressure at the interface between the two fluids. The pressure is non-dimensionalized by $\rho_a g_0' h_0$, and the other variables are scaled as before.

The depth and velocity of the ambient fluid can be written in terms of the variables that describe the gravity current. Because the total depth of the two layers is fixed, the dimensionless depths of the current and ambient layers are related by

$$h(x,t)+h_u(x,t)=1. \tag{22}$$

For a gravity current of fixed volume with no flow at the endwall ($x=0$), we can deduce from (17), (18) and (22) that

$$u(x,t)\,h(x,t)+u_u(x,t)\,h_u(x,t)=0, \tag{23}$$

which states that there is no net flux across any vertical cross-section.

Using (22) and (23) and adding linear combinations of (19) and (20) to eliminate the interfacial pressure, we can derive the combined two-layer momentum equation

$$\frac{\partial}{\partial t}(uh)+(1-h)\frac{\partial}{\partial x}[u^2h+\tfrac{1}{2}(\phi-\gamma)\,h^2]+h\frac{\partial}{\partial x}[uh(1-h)]=0. \tag{24}$$

Note that for a gravity current in very deep ambient fluid, $h\approx 0$, for which case the third term in (24) is negligible and the single-layer shallow-water momentum equation is recovered.

The two-layer model comprises the three equations (17), (21) and (24) for the three variables h, u and ϕ that describe the gravity current together with appropriate boundary conditions. Huppert & Simpson (1980) found that the Froude number at the nose varied in relatively shallow surroundings with the ratio of the height of the gravity current to the depth of the ambient fluid. Experimentally, they found that the dimensionless nose condition is

$$u_N = Fr[(\phi_N-\gamma)\,h_N]^{\frac{1}{2}},$$

where

$$Fr = 1.19 \quad (0\leqslant h_N\leqslant 0.075) \tag{25a}$$

$$= 0.5h_N^{-\frac{1}{3}} \quad (0.075\leqslant h_N\leqslant 1). \tag{25b}$$

This experimental correlation for the Froude number is qualitatively similar but always less than Benjamin's (1968) theoretical prediction for the Froude number at the front of a current that intrudes into shallow surroundings. The difference between the results is due to viscous drag and Reynolds stresses along the head of the current which increase the momentum loss at the front, as discussed earlier. The additional boundary condition is still zero flow at the endwall.

Rottman & Simpson (1983) solved similar two-layer shallow-water equations and boundary conditions numerically to study the slumping of a fixed-volume homogeneous gravity current and its transition to the long-time similarity solution. They were successful in modelling their experiments for initial values of the current depth less than or equal to about half that of the total depth. For greater initial depths, they were not able to include in their numerical scheme the bore that forms when the

overlying fluid that replaces the collapsing gravity current reaches the endwall. In the next section we briefly describe our method of numerical solution, which includes the equation of particle conservation and captures the formation of the bore.

3. Numerical results

3.1. *Numerical method*

When particles settle out of the current, that is for $\beta \neq 0$, there is no analytic solution to either the single- or the two-layer equations for a particle-driven gravity current, and so the equations must be solved numerically. The numerical method must be able to determine the position of the moving front or nose of the current and handle any shocks or jumps that occur in the system of hyperbolic equations.

We need to solve three simultaneous partial differential equations for the conservation of mass, momentum and particles in the current. In the single-layer model these equations are (7)–(9) subject to the boundary conditions (10) and (11); for the two-layer model they are (17), (21) and (24) subject to the two-layer nose and endwall boundary conditions. Because the front of the current translates, it is convenient to transform the spatial variable x to the new variable $y = x/x_N(t)$. The range of this new spatial variable is confined to $[0, 1]$, and the nose is fixed at $y = 1$. It is also more convenient to solve the equations for the conservative variables $h, q = uh$ and $\varphi = \phi h$. The transformed equations and their boundary conditions in the conservative variables for the single-layer model are given in (A 3)–(A 7).

These equations are solved using the two-step Lax–Wendroff method as outlined, for example, by Press *et al.* (1986, pp. 623–625). The method is explicit in its forward time integration at the differencing grid points in the interior of the domain, but there must be some additions to the method to compute boundary points. The boundary conditions provide one relationship at each end of the spatial domain of the flow; but clearly there are three dependent variables to be specified at each boundary, and so there must be two more equations at each boundary. These additional relationships are derived from the characteristic equations for the single- or the two-layer model. This technique for determining the end points of an explicit finite-difference scheme using the method of characteristics is described, for example, by Abbott & Basco (1989, pp. 225–234), and is discussed in greater detail in Appendix A. The velocity of the front at each time step is then determined by this technique and the length of the current is updated with a trapezoidal integrator. This numerical method is accurate to second order in both time and space.

Because the equations are hyperbolic, they can and, as we shall see, do admit shocks, and some modifications must be made to account for them. There is some numerical dissipation in the Lax–Wendroff method, but to ensure a smoother transition between supercritical and subcritical flow regimes, a small amount of extra dissipation is added to the momentum equation in the form of a bulk-viscosity term, as shown in (A 16). This term only becomes important where the gradients in velocity are very large and, other than smoothing out the shocks and decreasing overshoots in transitions, does not affect the dynamics of the flow.

3.2. *Profiles for a current in deep surroundings*

The height, velocity and concentration profiles for a particle-driven gravity current intruding into a deep ambient fluid are presented in figures 3 and 4. The fixed volume of fluid begins at rest and its length is initially one half the starting height. The settling

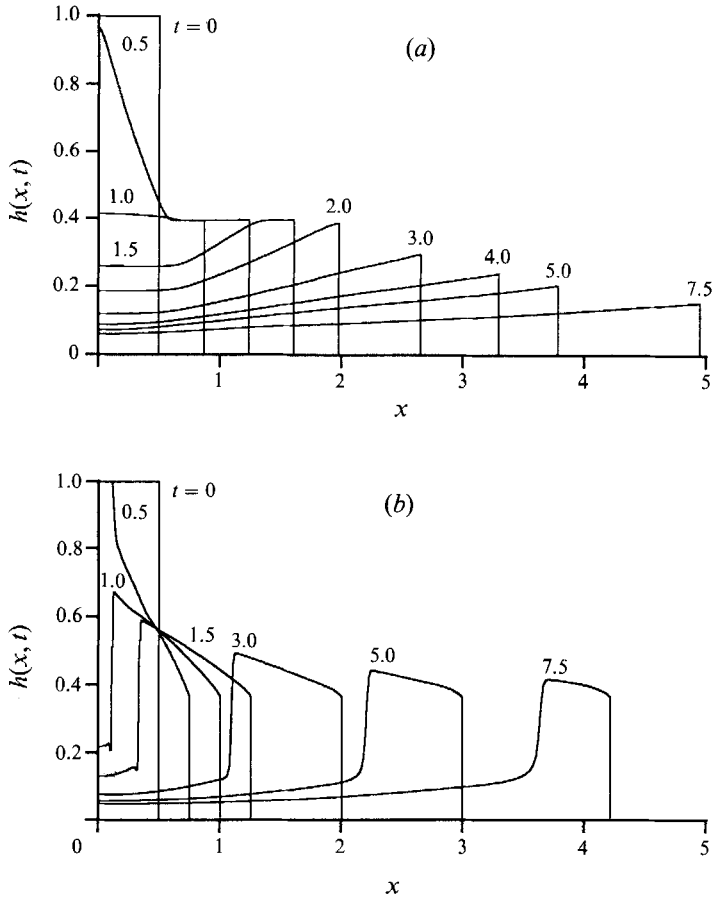

FIGURE 3. The numerically determined profiles of the height $h(x, t)$ of a collapsing particle-driven gravity current of fixed volume at early times intruding into: (*a*) a very deep body of ambient fluid; (*b*) a shallow body of ambient fluid. In each case the current is initially at rest and has a dimensionless volume per unit width $q = 0.5$ and a settling number $\beta = 5 \times 10^{-3}$. The successive times are noted next to each profile.

number β here is 5×10^{-3}, which is within the range of geological values for this parameter; for example, this value would be appropriate for a turbidity current with an initial volume fraction 5% of 200 μm-diameter sand and initial height of 20 m, for which $v_s = 2$ cm s^{-1} and $g_0' = 0.81$ m s^{-2}.

The dynamics of the current can be roughly divided into three phases: an initial or starting phase, during which the initially stationary fixed volume of fluid collapses and approaches the self-similar solution though very few particles have yet settled out of the current; a transition phase, in which the particles are preferentially removed from the rear of the current and the fluid in the tail decelerates less rapidly than the nose; and a travelling shock phase, during which a bore develops within the current and separates a particle-free jet region from a relatively particle-rich gravity-current region.

Figure 3(*a*) shows the height profiles in the starting phase of the current. The initially stationary fluid collapses from the front of the current, first creating a wave that a short time later is reflected from the endwall and travels towards the front. Meanwhile, the current lengthens as the front propagates and the height profile approaches the self-similar shape depicted in figure 2. During this phase very few particles settle out from

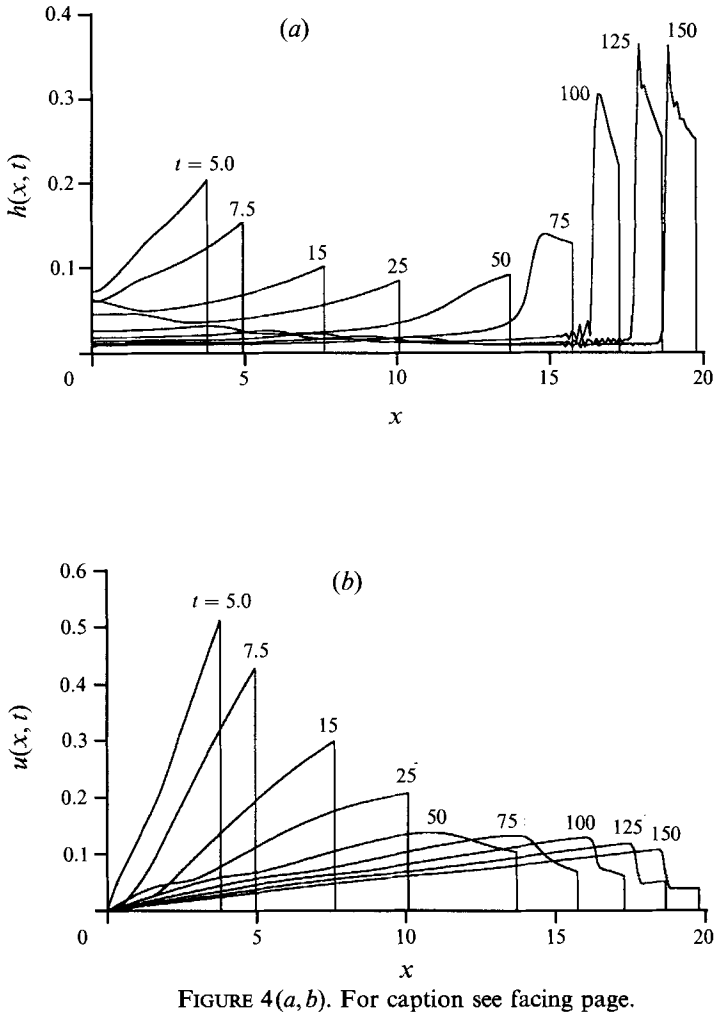

FIGURE 4(*a*, *b*). For caption see facing page.

the current, as may be seen from the particle concentration profile in figure 4(*c*) and the time trace of the total concentration in figure 8. In this initial phase the current behaves very much like a homogeneous current as described by Rottman & Simpson (1983).

As particles settle out from the current, however, the structure of the current changes markedly from the near self-similar form. Figure 4 shows the height, velocity and concentration profiles during the transition and travelling-shock phases. The height and velocity profiles look like the self-similar form until about $t = 15$. Shortly thereafter, the fluid behind the nose of the current no longer decelerates as rapidly as the nose and a maximum in the velocity appears. Meanwhile, during the transition phase, the height of the current near the front is increasing and the particle concentration is decreasing more rapidly in the rear of the current than near the front. Eventually, a distinct travelling shock or bore forms in the current, as seen by the very rapid transitions in the height and velocity. The overshoot in the height of the current and the small oscillations at the bore are due to the limitations of the numerical method in resolving the discontinuity, but do not change its characteristics very much. We note that the concentration of particles varies continuously across the shock by virtue of the

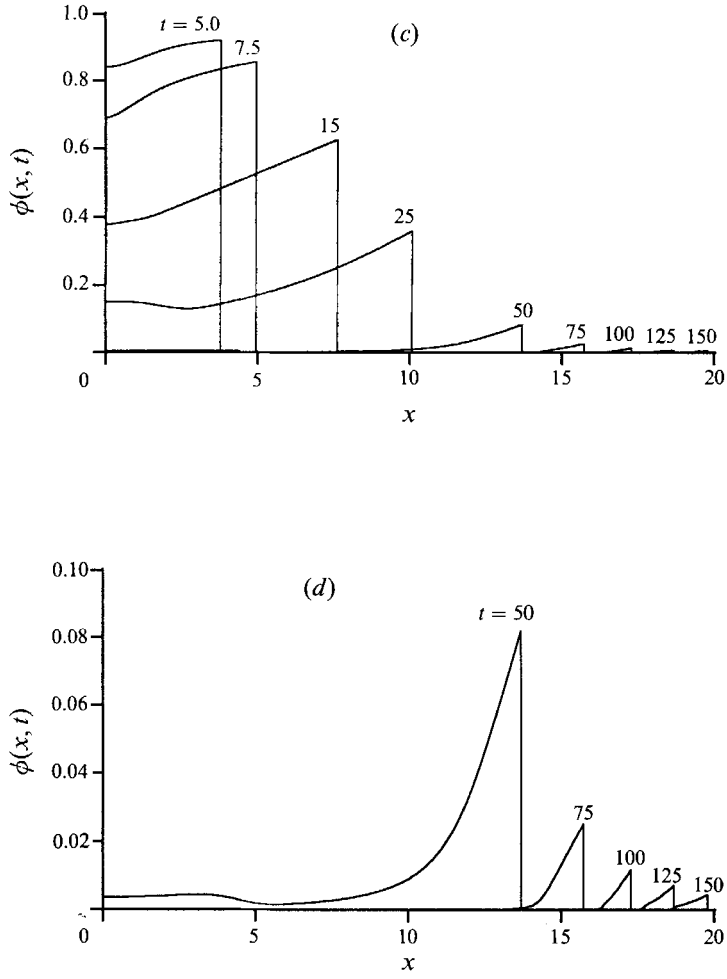

FIGURE 4. The numerically determined profiles at later times for the current described in 3(*a*). Illustrated are (*a*) the height $h(x,t)$; (*b*) the velocity $u(x,t)$; and (*c*) and (*d*) the volume fraction of particles $\phi(x,t)$ with two different scales.

conservation of particles and fluid. At this stage the fluid in the rear of the shock is effectively particle-free and the fluid in front is relatively particle-rich.

The formation of the travelling shock is due to the differential settling of particles along the length of the current. We recall that the variation in the height from the head to the tail of the current establishes a pressure gradient that decelerates the fluid behind the nose. The particles settle out more rapidly towards the rear of the current, due to the smaller height there, and consequently the density and pressure gradient in the tail is reduced. Thus, the rearward fluid is not decelerated sufficiently rapidly to maintain the self-similar profile. As a result, the rearward fluid accumulates behind the head due to the slower movement of the nose. The particle concentration in the tail virtually vanishes, and the flow there is like a jet, since the motion is due to the momentum of the particle-free fluid and the effects of buoyancy are negligible. Near the front, the current is still relatively rich in particles, though the concentration is small compared to the initial value, and so it continues to behave like a buoyancy-driven flow. The travelling shock is a consequence of matching of the jet-like flow in the rear of the

current to the buoyancy-driven flow in the front. The shock equations are those for the shallow-water equations with the density of the current written as a function of the particle concentration.

The shock propagates forward and eventually comes sufficiently close to the front that our numerical method with a fixed number of spatial grid points in y can no longer resolve it. A finer discretization near the front could be used to extend the computations, but it is not practically worthwhile. The initial suspension of an experimental current, as described below, contains some fine particles, and when the concentration near the front becomes very low in the shock phase, those fines that remain in suspension probably dominate the behaviour of the current but are not accounted for in the model.

While the division of the evolution of the current into three phases is convenient, it is also somewhat arbitrary. Depending upon the value of β, the first two phases may in fact overlap. For example, if β is large the particles settle out rapidly as the current collapses, and the shock develops immediately. The values for the settling number in our experiments are in the range of 10^{-4} to 10^{-2}, and estimates for some geological-scale particle-driven gravity currents are in a similar range. Thus the sequence of events shown here is probably not uncommon for such a current intruding into deep surroundings.

3.3. *Profiles for a current in shallow surroundings*

A gravity current of fixed volume can be generated by removing a gate separating a volume of dense fluid from lighter ambient fluid. It has been observed that if the initial height of the gravity current is more than 70% of the depth of the ambient fluid, the current does not merely collapse and approach the self-similar flow, but that another gravity current comprising the ambient fluid moves over the dense underflow in a lock-exchange flow until it reaches the endwall. A bore is then reflected towards the front which it eventually overtakes. The underlying current then continues its intrusion into the ambient fluid.

This sequence of events is illustrated both experimentally and numerically in the photographs and height profiles in figure 5. The experimental photographs (from Rottman & Simpson 1983) and numerical profiles are for a saline current with an initial height equal to the ambient fresh water depth of 7 cm, an initial length of 50 cm, and a value of the reduced gravity $g' = 47$ cm s^{-2}. The sequence of events determined from the numerical solution of the two-layer model equations shows almost the same quantitative behaviour as seen in the experiment. The distance downstream of the nose of the gravity current is predicted quite accurately. The fresh water is predicted to flow over the gravity current slightly faster in the lock-exchange phase of the flow than is observed experimentally. This is probably because no viscous resistance is included for the gravity-current-like flow of the ambient fluid. The bores in the last two numerical profiles have propagated slightly further than in the experiments, but this is due to the greater speed of the surface current and its earlier reflection in the numerical simulation. The distance between the experimental and numerically observed bores, however, is about the same.

Rottman & Simpson (1983) tried to use the two-layer shallow-water equations to model this bore formation in a homogeneous gravity current. They used the method of characteristics to solve the equations and found it rather difficult to fit the shock into the solution since it is necessary to apply the shock equations relating to conjugate states (of which there are four for this system!) and match them to the flow. However, our method is well adapted for shock resolution since it computes the shock and its dynamics as part of the solution. The accurate comparison between the experiment of

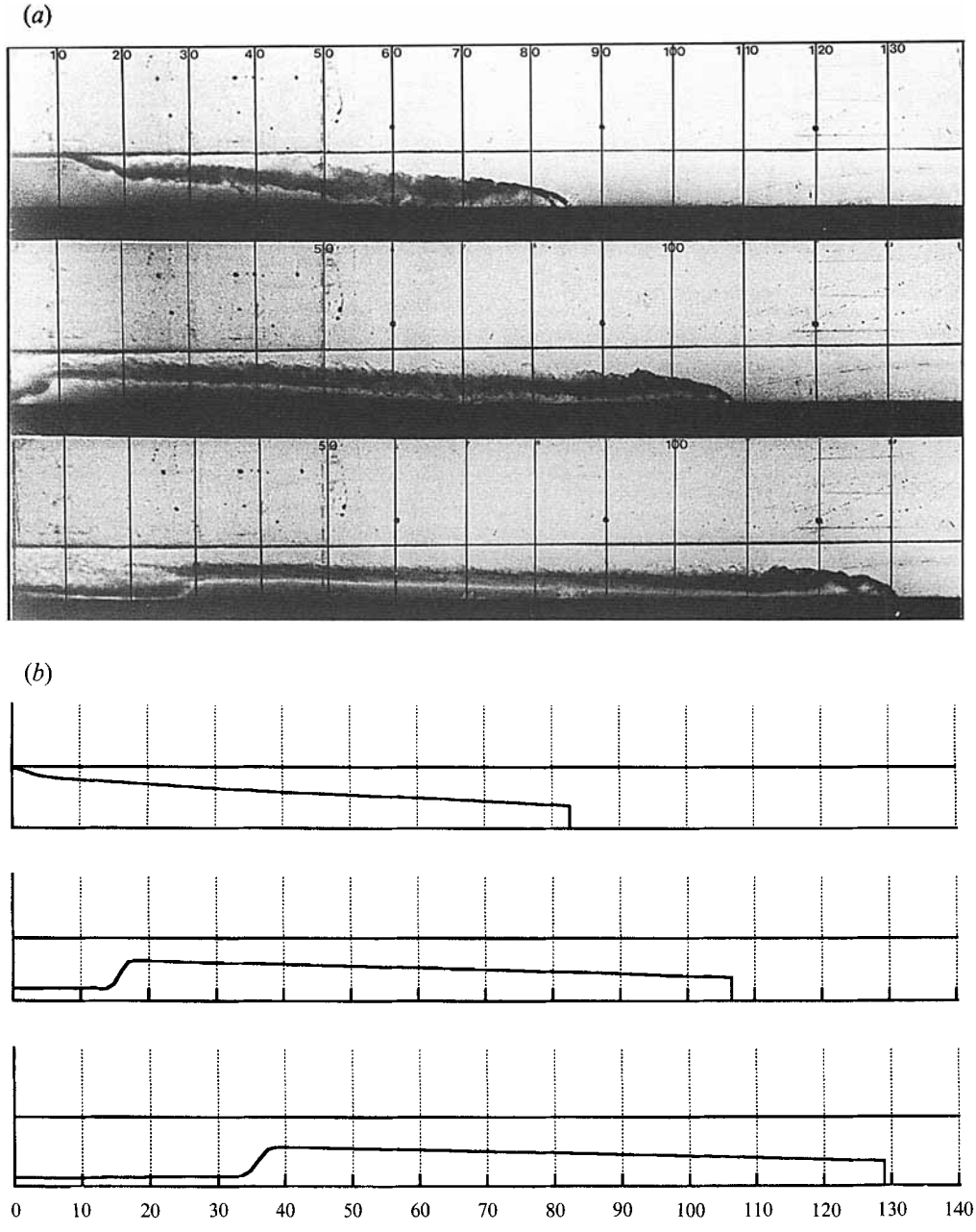

FIGURE 5. (*a*) Shadowgraphs of a homogeneous gravity current of salt water collapsing in a shallow body of fresh water from Rottman & Simpson (1983). The initial dimensions of the current are $h_0 = 7$ cm and $x_0 = 50$ cm with the reduced gravity $g' = 47$ cm s^{-2}. The vertical lines indicate positions in the tank and are at 10 cm intervals. (*b*) Numerically determined profile of the same current using the two-layer model. The good agreement between the numerical and experimental results is clearly evident.

Rottman & Simpson and our calculations is one verification of our model and the numerical technique.

For a particle-driven current collapsing into a relatively shallow fluid, the sequence of events is initially rather similar to that for the homogeneous current in figure 5.

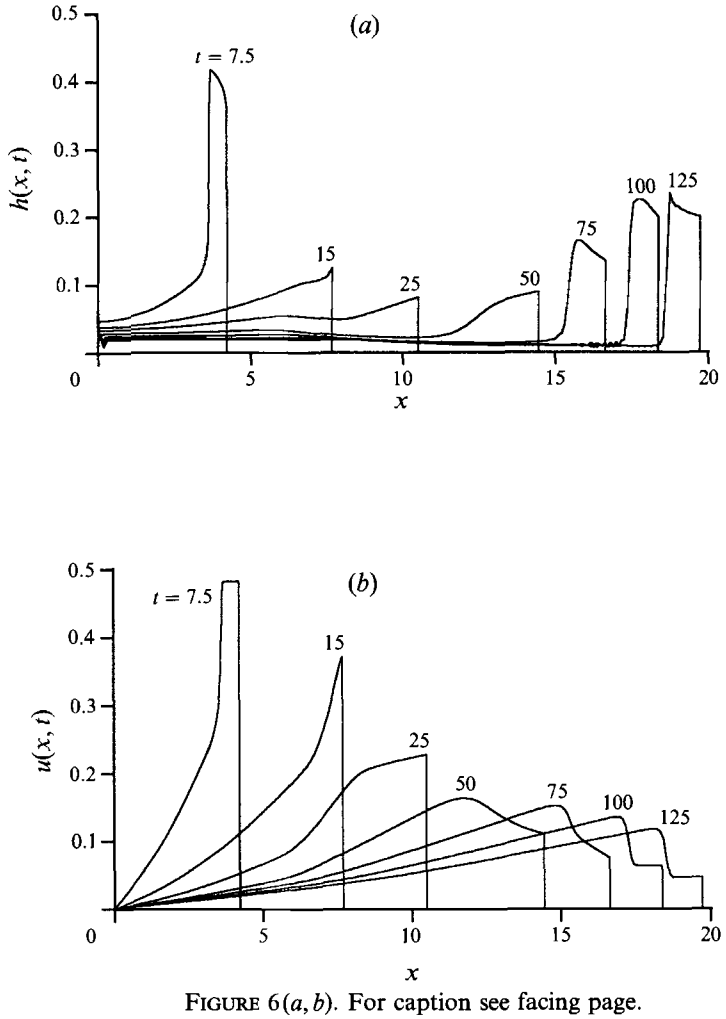

FIGURE 6(*a*, *b*). For caption see facing page.

Figures 3(*b*) and 6 present the height, velocity and concentration profiles for an initially stationary fluid with a starting height equal to the depth of the surrounding fluid and a settling number $\beta = 5 \times 10^{-3}$. Again, the dynamics of this current can be conveniently divided into three phases: a slumping phase, during which the current collapses and the bore between the ambient and current fluid forms; a transition phase, in which the first bore vanishes and the internal bore begins to appear; and finally the internal travelling bore phase already noted.

Figure 3(*b*) depicts the height profile for the gravity current at early times. As in the homogeneous example in figure 5, a bore forms after the overlying gravity current composed of ambient fluid reaches the endwall. The bore is similar to the wave reflected from the endwall for the current intruding into deep surroundings in figure 3(*a*). The height of the current behind the bore, however, is much shallower than the depth of the current in the other case. The height of the front also remains constant as the bore travels towards the nose of the current, unlike the current collapsing into deep surroundings. Eventually the bore reaches the front of the current and, as seen in figure 6, the rearward fluid begins to catch up with the nose and the height near the front begins to increase. An internal travelling shock develops within the current, which, as

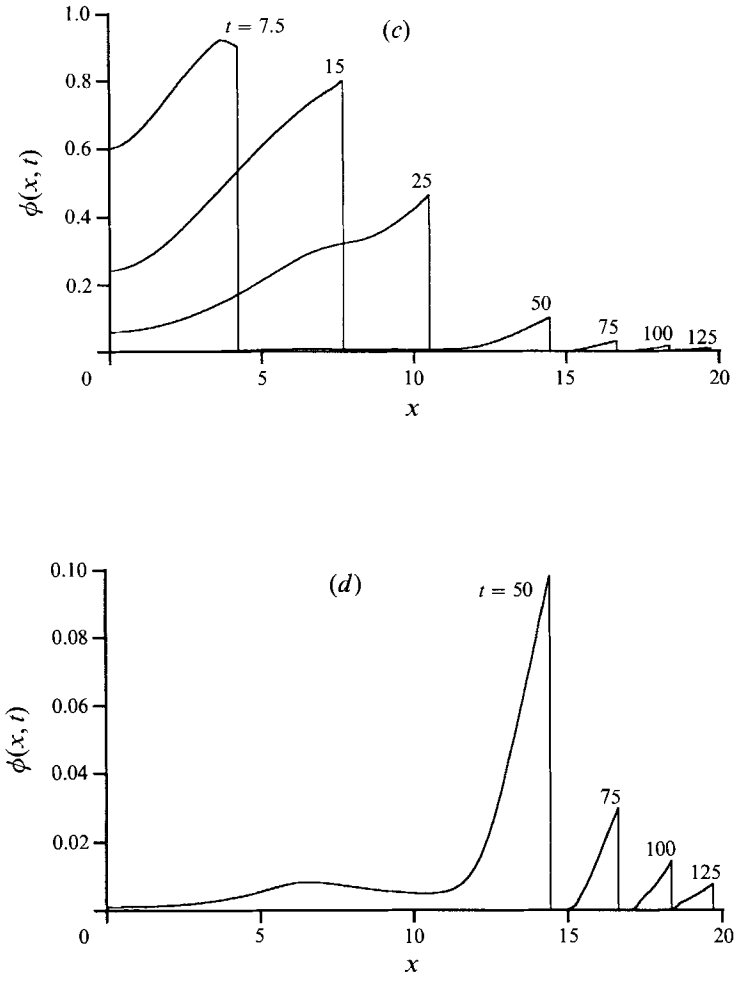

FIGURE 6. The numerically determined profiles at later times for the current described in 3(*b*). Illustrated are (*a*) the height $h(x, t)$; (*b*) the velocity $u(x, t)$; and (*c*) and (*d*) the volume fraction of particles $\phi(x, t)$ with two different scales.

before, separates a particle-free jet region in the rear from a relatively particle-rich region near the front.

Clearly, the initial collapse of a particle-driven gravity current is very different depending on whether it is intruding into relatively shallow or deep surroundings. Further, although the transition and travelling-bore phases are qualitatively similar for the two conditions, the length of the current as a function of time and the particle distribution within the current remain noticeably different.

Figure 7 compares the lengths of currents as a function of time for the two particle-driven gravity currents and two homogeneous currents, with the same initial densities, intruding into either deep or shallow surroundings. Not surprisingly, the lengths of the particle-driven currents at early times are the same as the equivalent homogeneous currents because very few particles have settled out of the suspension. At later times, the lengths of the particle-driven currents are less than their homogeneous counterparts because the loss of particles reduces the buoyancy driving force at the nose. For flows either with or without particles, the length of the current intruding into the deeper

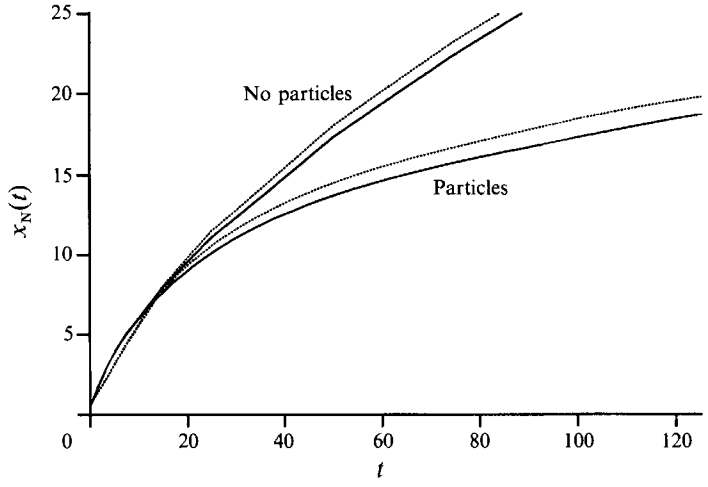

FIGURE 7. The numerically determined length as a function of time for homogeneous and particle-driven gravity currents. The dimensionless volumes per unit width of the currents are $q = 0.5$ with an initial height of unity and length of one half. The initial reduced gravity for the particle-driven current is the same as that of the homogeneous current. The settling number for the particle-driven current is $\beta = 5 \times 10^{-3}$. The upper pair of curves are for a homogeneous current and the lower pair are for a particle-driven gravity current. The solid curves were computed using the single-layer model and the dotted curves using the two-layer model.

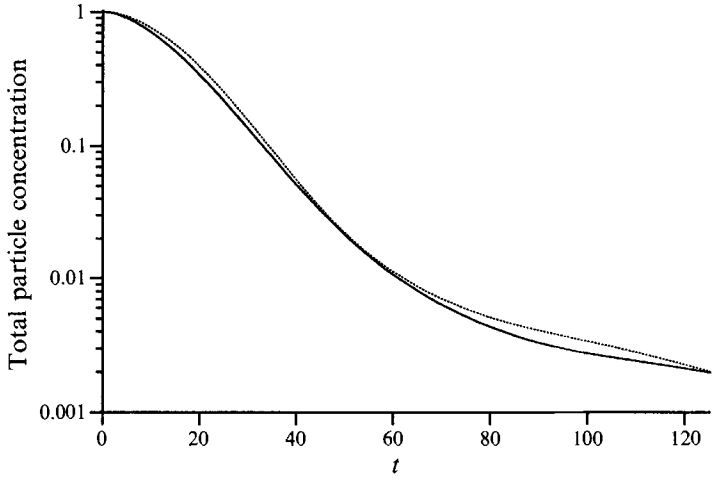

FIGURE 8. The total integrated volume fraction of particles as a function of time for the gravity currents described in figure 3. The solid curve is for a current intruding into a deep body of ambient fluid and the dotted curve is for a current intruding into a shallow body of ambient fluid.

surroundings initially increases in proportion to $t^{\frac{2}{3}}$ while the length of the current in shallow surroundings initially increases in proportion to t, due to the bore which maintains a constant height and velocity at the nose. Subsequently, there is a cross-over in the lengths. Once the bore reaches the front of the currents in shallow surroundings, the velocities of the currents are about the same, though the lengths of the currents in shallow surroundings are greater than their counterparts in deep surroundings.

The total concentration of particles as a function of time for the two sediment-laden currents are compared in figure 8. The differences are rather small, with the current in shallow surroundings having a slightly higher concentration of particles. The bore that

occurs for the current in shallow surroundings, however, strongly affects the deposition pattern of the sediment. This is discussed in the following section, in which we compare our numerical predictions with experimental measurements. We also consider the effects of the value of the settling number on the length of the current as a function of time and on the deposition patterns.

4. Experiments

We performed several experiments with particle-driven gravity currents to determine both their lengths as a function of time and the resulting areal density of their deposits. The experiments were performed in a glass tank 10 m long, 26 cm wide and 48 cm deep. The tank was filled to a height of 30 cm with tap water. A Perspex gate with foam seals around its edges was placed 15 cm from the endwall, so that the volume of fluid behind the gate was 11 700 cm^3.

The suspension for the current was made by mixing fairly monodisperse, non-cohesive silicon carbide particles in the water behind the gate. As a precaution, a small amount of Calgon was added to ensure the particles would not coagulate. The mean particle sizes ranged from 9 to 53 μm and all particles had a density of 3.217 g cm^{-3}. The total mass of solids initially suspended varied from 100 to 800 g while the volume fraction of particles in the suspension was always less than 2%. This is consistent with the assumption in the model that $\phi \ll 1$. The initial values of the reduced gravity of the currents ranged from 5.7 to 45.8 cm s^{-2}.

After the suspension of particles had been well-mixed, the gate was lifted to release the gravity current. As the current propagated down the tank, the position of its front was marked on the glass wall of the tank at 5 or 10 s intervals and the distance from the end of the tank was recorded at the conclusion of the experiment. In several cases, after the current had reached the end of the tank, the surface density of the deposit was measured along the length of the tank. A Perspex cylinder with an internal diameter of 9.35 cm was centred on the bottom of the tank at specific locations along the tank, and all the sediment within it was 'vacuumed up' with a siphon tube. The particles were collected in a beaker, the water decanted and the particles dried and weighed to determine the mass of deposit per unit area. As a check on the method for collecting the sediment, the total mass of sediment was calculated by integrating the measured deposition profile. The calculated value was always within 5% of the actual initial weight of particles in the suspension, which confirmed the accuracy of the vacuuming technique.

A series of photographs of a typical particle-driven gravity current is shown in figure 9(*a*). In order to photograph the entire current, these were taken in a smaller tank, but the behaviour of the current is similar to that in the large tank for all the other experiments. The current was composed of 75 g of 53 μm-diameter particles mixed behind a gate 8 cm from the back wall of the tank, which was 27 cm wide and filled to a depth of 14 cm. The initial value of the reduced gravity was 15.2 cm s^{-2}. After the gate was removed, the front propagated downstream and the bore quickly developed and moved towards the front. The precise location of the shock is difficult to determine since there is some shedding of the dyed interstitial fluid from the back of the bore. Figure 9(*b*) shows plots of the height of the current from numerical integration of the two-layer model. The predicted lengths of the current agree well with the photographs though, as already discussed in regard to the saline current in figure 5, the bore is predicted to form sooner than observed and thus appears further downstream. The weak shock at 21 s shown in the numerical prediction is the beginning of the internal

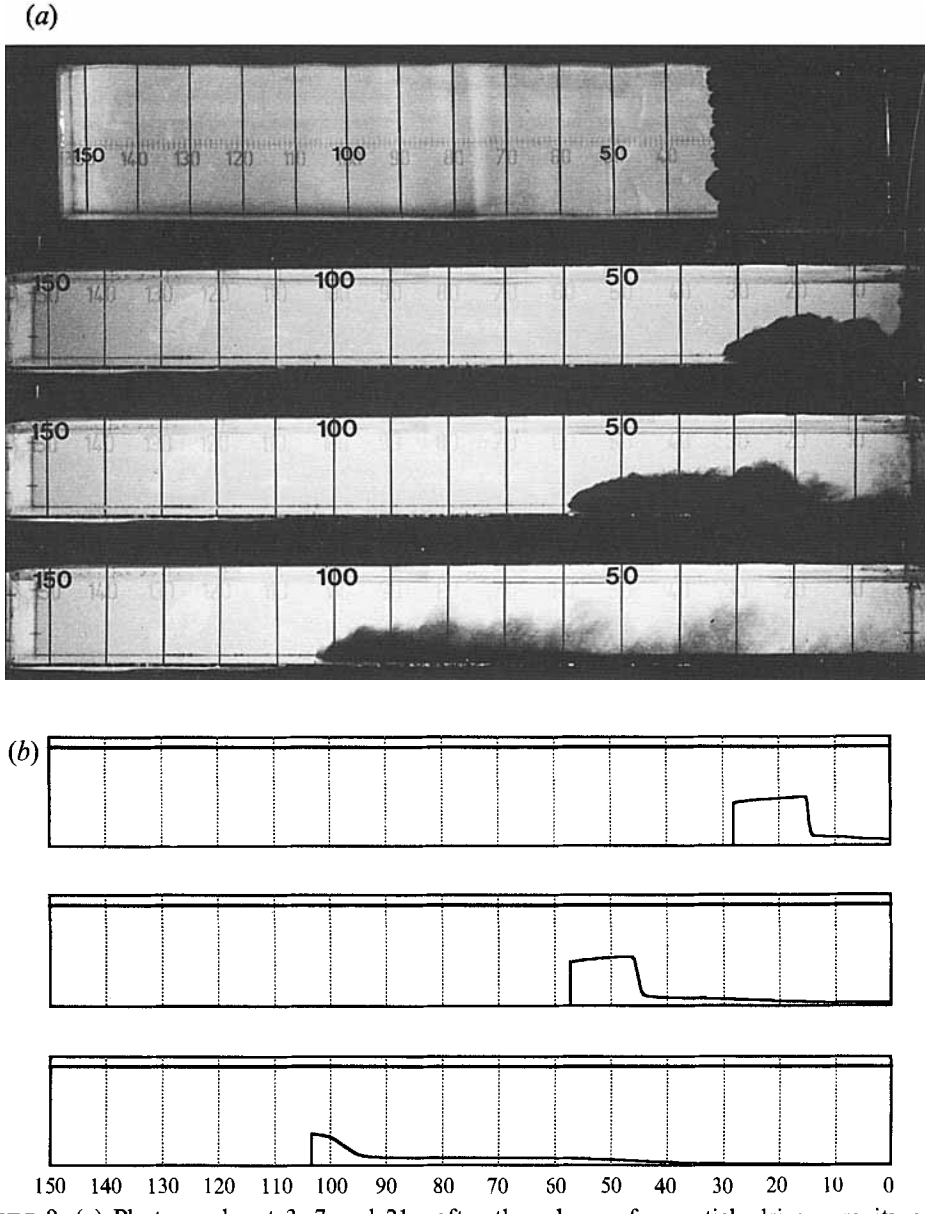

FIGURE 9. (*a*) Photographs at 3, 7 and 21 s after the release of a particle-driven gravity current composed of 75 g of 53 μm particles. The initial dimensions of the current are $h_0 = 14$ cm and $x_0 = 8$ cm with a value of the reduced gravity $g' = 15$ cm s^{-1}. The upper photograph is a top view of the first of the sequence, which shows the two-dimensional nature of the flow and the negligible effect of the sidewalls. (The tank is 27 cm wide.) (*b*) The numerical predictions of the height and length of the current from the two-layer model at the same times as the photographs in (*a*). There is fairly good quantitative agreement between the predicted and observed structure of the current at each time.

travelling shock that forms in the later stage of the flow of particle-driven gravity currents, and such a structure arguably appears in the corresponding photograph.

Figure 10 presents the lengths as functions of time for particle-driven gravity currents with initial loads of sediment of 400 g and particle sizes of 9, 23, 37 and 53 μm. The length as a function of time is also presented for a saline current with the same

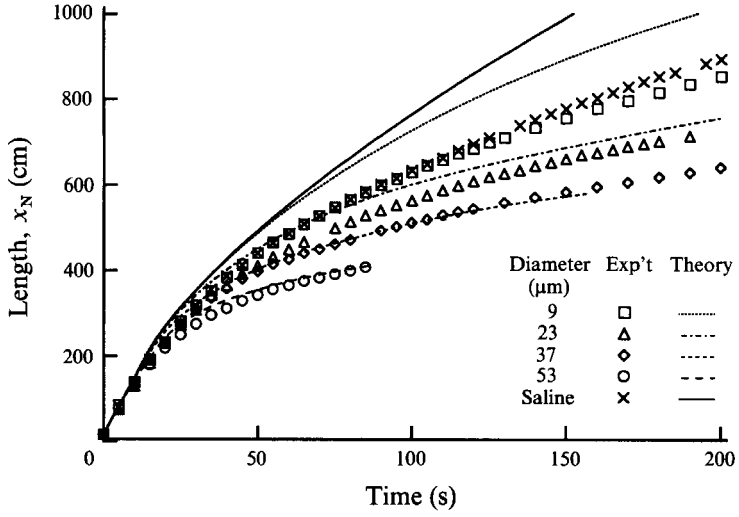

FIGURE 10. The length as a function of time for gravity currents composed of suspensions of silicon carbide particles or of salt solutions released into a tank of fresh water. The initial dimensions per unit width of the currents was 30 cm high × 15 cm long. The depth of the water in the tank was 30 cm and the initial reduced gravity for all the currents was 22.9 cm s^{-2}. The symbols are from experimental measurements and the curves are from the numerical solution of the two-layer model. The particle sizes are listed on the figure.

initial value of reduced gravity 22.9 cm s^{-2}. At early times the lengths of all these currents were identical, because very few particles had settled out of the particle-driven currents. In fact the lengths grew linearly with time while they were in the slumping phase, as discussed earlier. At later times the lengths of all the currents increased more slowly, and the length of the saline current exceeded that of the particle-driven currents, which decreased with increasing particle size. The larger particles settled out more rapidly, thus reducing the density difference between the current and the ambient fluid and hence the driving buoyancy force.

Also plotted in figure 10 are the theoretical predictions of the two-layer model for the lengths of the currents as a function of time. For all but the smallest particle size and the saline current, the agreement between the theory and experiments is very good. In the cases of the saline current and the current with 9 μm-diameter particles, the agreement is initially very good while the inertial forces dominate the viscous forces, but at long times the viscous forces are no longer negligible, and this effect is not included in our model.

It is curious that the inertial forces dominate the dynamics of most of the particle-driven gravity currents for so much longer than the saline current. To understand this and to determine the time limit of validity for the model, we need to know when a particle-driven gravity current makes the transition from an inertial–buoyancy balance to a viscous–buoyancy balance.

The time for transition from one regime to the other has been determined experimentally by Huppert & Simpson (1980). They found for a homogeneous gravity current that the dimensional time, t_c, when the current changes from inertial to viscous flow is given by

$$t_c = 0.5(q^4/\nu^3 g'^2)^{\frac{1}{7}}, \tag{26}$$

where ν is the kinematic viscosity and q is the volume per unit width of the current. Because the reduced gravity g' is time-dependent for a particle-driven gravity current,

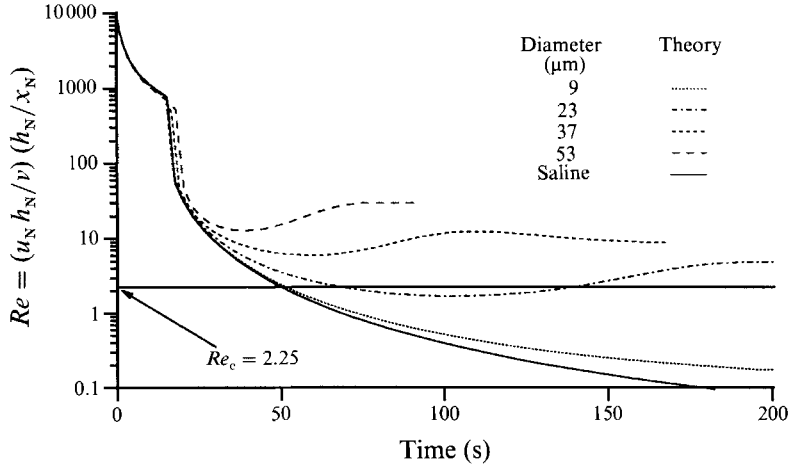

FIGURE 11. The time trace of the Reynolds number $Re = (u_N h_N/\nu)(h_N/x_N)$ computed by the two-layer model for the gravity currents in figure 10. When the Reynolds number is greater than the critical value of 2.25, the current is dominated by an inertial–buoyancy balance, and below that value viscous forces dominate the inertial forces and our models are no longer applicable.

it is more convenient to have a criterion in terms of a Reynolds number, Re, which quantifies the relative importance of inertial to viscous forces in the current. From the time of transition we show in Appendix B that the critical Reynolds number, Re_c, below which the viscous forces dominate is

$$Re_c = 2.25, \tag{27}$$

where

$$Re = (u_N h_N/\nu)(h_N/x_N) \tag{28}$$

in terms of the height and velocity at the nose.

The values of the Reynolds numbers computed from the model for the currents in figure 10 are shown in figure 11. The Reynolds numbers for all the currents are largest in the initial phase during which their fronts are moving most rapidly and their lengths are shortest. The Reynolds number decreases as the current lengthens and then drops dramatically at the time when the initial bore reaches the nose of the current. Until this point the height and velocity at the nose are constant and the Reynolds number decreases only because the length of the current is growing. After the bore has reached the nose, the Reynolds number decreases due to the now decreasing velocity and height at the front as well as to the growing length of the current. For particle-driven currents, the Reynolds number has a shallow minimum followed by a slightly larger, almost plateau, value. The minimum in the Reynolds number reflects the minimum in the height at the nose as seen in the profiles in figures 4 and 6. At large times the Reynolds number is greater for the particle-driven currents than for the homogeneous current due to the relatively larger height at the front and to the shorter length.

For the saline current and for the current with 9 μm-diameter particles, the Reynolds number drops below 2.25 and into the viscous regime after about 50 s. This is also the time when the theoretical prediction of the length deviates above the experimental value because of this transition. The current with 9 μm-diameter particles effectively behaves like the saline current, because the particles have a small settling velocity and very few have settled out in the first 200 s. For the other particle-driven currents, the Reynolds number is always sufficiently large to ensure that the dynamics of the current are dominated by inertial forces rather than by viscous forces. For the current with

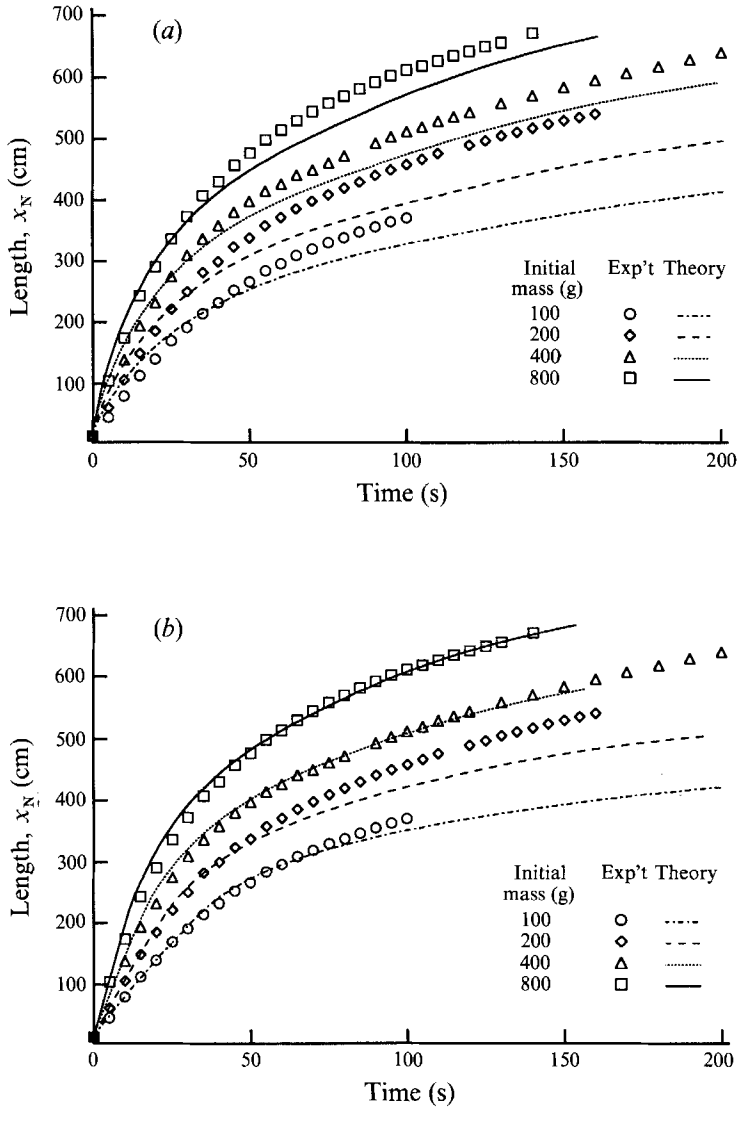

FIGURE 12. The length as a function of time for particle-driven gravity currents composed of suspensions of nominally 37 μm diameter particles with varying initial masses of sediment. The symbols are the experimental measurements and the curves are numerical predictions using: (*a*) the single-layer model; (*b*) the two-layer model. The initial masses are listed on the figure.

23 μm-sized particles, the Reynolds number dips slightly below Re_c for a time, which is consistent with the small deviation between the theory and the experiment in figure 10.

The initial mass of sediment was also varied between 100 and 800 g for a suspension of particles that had a nominal diameter of 37 μm. The lengths of the currents as functions of time are presented in figure 12 along with the theoretical predictions from both the single-layer and two-layer models. Clearly, the two-layer shallow-water equations are superior for modelling the experiments, and the agreement between the theoretical and experimental points is extremely good. The two-layer model captures the initial slumping behaviour and the long-time motion of the front of the current as well.

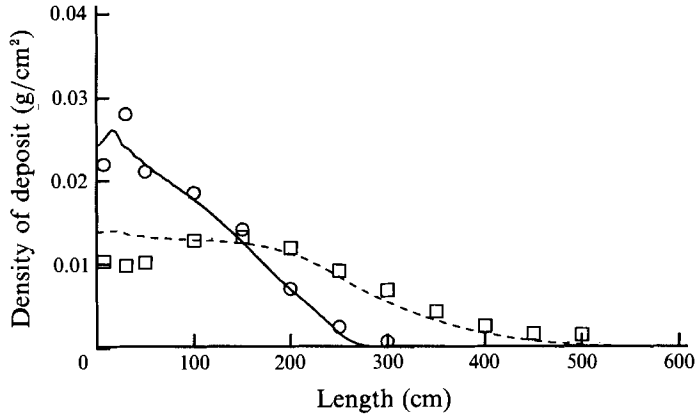

FIGURE 13. The final areal density of the deposit after the flow of particle-driven gravity currents with an initial mass of 100 g of sediment for two different particle sizes. The curves are the numerical predictions from the two-layer model, and the symbols are the experimental measurements for: (*a*) 23 μm diameter (open squares and dotted line); (*b*) 53 μm diameter (open circles and solid line).

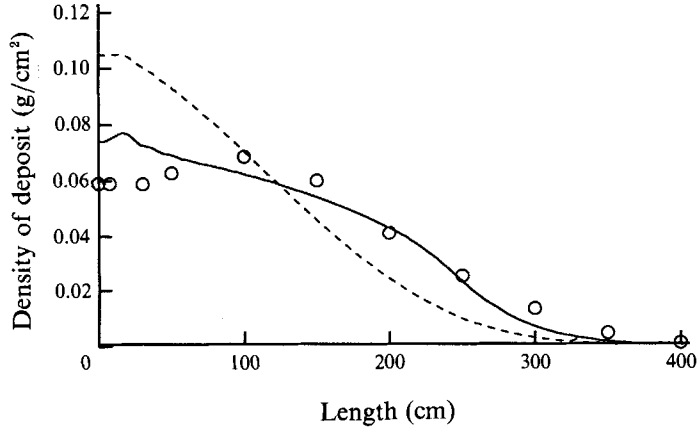

FIGURE 14. The final areal density of deposit after the flow of particle-driven gravity currents with an initial mass of 400 g 53 μm-diameter particles. The curves are the numerical predictions from the single-layer model (dotted line) and the two-layer model (solid line), and the symbols are the experimental measurements.

Typical areal densities of the deposit as a function of the downstream distance are presented in figures 13 and 14. The experimental densities of the deposit profile increase from the wall to a maximum value and then decrease towards zero. The magnitude of the maximum in density depends on the particle size, and the deposits of smaller particles have a slightly larger maximum than the deposits with the larger particles. The predicted values of the density of deposits from the two-layer model are also illustrated, and they match the measured values very closely.

Also included in figure 14 is the prediction of the deposition from the single-layer model. Both theoretical curves show the density of the deposit decreasing downstream, but the predictions from the two-layer model are lower at the endwall and decrease less rapidly than those of the single-layer model. The difference in the patterns of deposition is due to the initial bore and to its effects on the sedimentation rate in the two-layer system. When the bore forms, most of the fluid of the current accumulates in front of this travelling shock, and so the height of the current near the nose is greater

than that predicted by the single-layer model. The greater height reduces the settling rate so that particles are advected further downstream, as is clearly shown by comparison of the two theoretical predictions of the deposition.

In some cases, there is a maximum in the density at about 100 cm downstream of the endwall, which neither model predicts. We suspect that when the current collapses and the initial bore appears, the flow may be sufficiently fast and turbulent to sweep sedimented particles downstream, but not so vigorous as to lift many particles back into the current. The maximum does not appear for the current with initially 100 g of 53 μm particles (figure 13), probably because the particles are too heavy to be swept forward by the flow which is relatively weaker than the current with initially 400 g of particles (figure 14). But, despite this unaccounted for transport in the deposit, the agreement between the predictions of the two-layer model and the measurements from the experiments is remarkably good.

5. Discussion

We have presented a successful model for describing the dynamics and deposition of a particle-driven gravity current of fixed volume. The dynamics of the current are controlled by a balance between the inertial forces of the flowing fluid and the buoyancy forces derived from the suspension of dense particles. The flow of the current is described with shallow-water equations, which are derived from the usual hydraulic assumptions of vertically uniform flow and a hydrostatic pressure distribution within the current, and include the contribution from the concentration of particles. Entrainment or detrainment of fluid at the top of the current is taken to be negligible. The particles are transported within the current by advection, and they settle out through a viscous sublayer at the bottom of the current without re-entrainment. At any position along the current the concentration of particles is assumed vertically uniform due to turbulent mixing.

The motion of any inertial gravity current is strongly controlled by the front, and we expressed this by the relationship between the velocity and the square root of the pressure head, $u_N = Fr(\phi_N h_N)^{\frac{1}{2}}$. This boundary condition represents the resistance to the motion of the head due to the inertia of the ambient fluid and viscous drag and turbulent Reynolds stresses on the head of the current. (The effects of drag forces are assumed only to be important at the head in so far as they change the value of the Froude number, Fr.) The Froude number at the head can vary with the ratio of the depth of the current to the depth of the surrounding fluid.

Our results show that when the depth of the current is comparable to the depth of the ambient fluid, such as in our experiments, the dynamics of the fluid overlying the current must also be included in the model. The same hydraulic assumptions are applied, and the equations of mass and momentum conservation of the overlying fluid are now coupled to the flow of the current. The model is only slightly more complicated, but the improvement in comparisons between the theoretical predictions and our experimental results is substantial.

The numerical solution of the model equations shows that two types of travelling shocks can occur in particle-driven gravity currents. An internal travelling shock occurs in the latter stages of the propagation, computed with either the single- or two-layer model, which separates a particle-free jet-like flow in the rear of the current from a dense, buoyancy-driven flow near the front. The other type of bore occurs only in the initial or slumping phase of currents that have an initial height equal to the depth of the surrounding fluid. This bore occurs irrespective of whether the current is

homogeneous or particle-driven, but it strongly affects the particle transport and the dynamics of the current for the latter type. Indeed it is the more important shock for modelling the experiments and is particularly critical for the accurate prediction of the deposition patterns of the sediment as seen in figure 14.

The agreement between the theoretical predictions using the two-layer model and the experimental measurements for the length of particle-driven currents as functions of time and their deposition patterns is very good. The agreement is especially significant because our model has no adjustable parameters. The Froude-number condition at the nose is determined from previous independent experiments on homogeneous gravity currents, and the settling velocity is just that determined from theoretical Stokes flow around spherical particles.

The present model can easily be modified to include concentrated suspensions and polydispersity. In our experiments the concentration of the particles was sufficiently dilute that the appropriate settling velocity for the model was that of an isolated particle. Correlations for the settling velocity of more dense suspensions that depend upon the concentration, however, could easily be included in our model. A current with a polydisperse suspension could be modelled by a discrete distribution of particle sizes, each of whose volume fraction obeys equation (4) for the conservation of particles with the appropriate settling velocity.

There are several phenomena which have not been analysed here that can be important in the flow of some natural gravity currents. As mentioned earlier, in particle-driven gravity currents with reversing buoyancy, the interstitial fluid is less dense than the ambient fluid so that, when sufficient particles have settled out, the bulk density of the current becomes less than that of surroundings, and the current rises like a buoyant plume. The point of liftoff for these currents has been discussed and predicted reasonably well by Sparks *et al.* (1992) using the model described here with a positive value for γ and some adjustments to account for the onset of buoyancy within the current.

Other interesting influences on the motion of gravity currents that can be included within the framework of our model include the effects of a slope with the additional acceleration due to the component of gravity. Indeed, for flows down a slope, the drag on the current due to the rigid boundary and the entrainment of ambient fluid can also be very important, as has been pointed out by Ellison & Turner (1959). These too can easily be included in our model with the friction factors and entrainment correlations taken from experimental results of previous studies. The entrainment of particles and the other processes mentioned are critical to the dynamics and deposition of, for example, ignited turbidity currents (Parker, Fukushima & Pantin 1986) flowing down erodable slopes, which occur in marine environments. Our future work on particle-driven gravity currents will explore all these effects, which can be incorporated within the structure of the model presented here.

We wish to thank Steve Sparks for many stimulating conversations, Mark Hallworth and Heidy Mader for assistance with the experimental measurements and John Simpson for kindly providing the photograph in figure 5. We are also grateful for helpful comments on an earlier draft of this manuscript from Ross Kerr and Nick McCave. This research has been partially supported by a grant from Venture Research International.

Appendix A. Numerical techniques

The equations and boundary conditions describing the dynamics of the flow and the transport of sediment in a particle-driven gravity current must be solved numerically for both the single-layer and the two-layer models. There are two aspects of the problem that make it interesting numerically. First, the front of the current is a moving boundary and its position must be determined as a function of time along with the rest of the flow field. Second, the equations are hyperbolic and thus admit shocks or discontinuities, and some allowances for them must be made in the numerical method. Here we address both these issues and outline a method for the numerical solution of the equations for the particular case of the single-layer model. The same techniques, though, are easily extended to the two-layer model.

A.1. *Moving front and numerical method*

Because the front of the current is moving and the Froude-number condition must be applied at the nose, it is more convenient to transform the equations from the (x, t) to a (y, τ) coordinate system, where $y = x/x_{\mathrm{N}}(t)$ and $\tau = t$. This maps the spatial domain to the finite interval $[0, 1]$ and the position of the front to the fixed point $y = 1$. The differentials are then given by

$$\frac{\partial}{\partial t} = \frac{\partial}{\partial \tau} - \frac{y\dot{x}_{\mathrm{N}}}{x_{\mathrm{N}}}\frac{\partial}{\partial y} \tag{A 1}$$

and

$$\frac{\partial}{\partial x} = \frac{1}{x_{\mathrm{N}}}\frac{\partial}{\partial y}. \tag{A 2}$$

Applying these differential transforms to (7)–(11) in terms of the conservative variables $h, q = uh$ and $\varphi = \phi h$, we find the equations for the single-layer model are

$$\frac{\partial h}{\partial t} = \frac{1}{x_{\mathrm{N}}}\left\{y\dot{x}_{\mathrm{N}}\frac{\partial h}{\partial y} - \frac{\partial q}{\partial y}\right\}, \tag{A 3}$$

$$\frac{\partial q}{\partial t} = \frac{1}{x_{\mathrm{N}}}\left\{y\dot{x}_{\mathrm{N}}\frac{\partial q}{\partial y} - \frac{\partial}{\partial y}\left(\frac{q^2}{h} + \tfrac{1}{2}[\varphi h - \gamma h^2]\right)\right\}, \tag{A 4}$$

$$\frac{\partial \varphi}{\partial t} = \frac{1}{x_{\mathrm{N}}}\left\{y\dot{x}_{\mathrm{N}}\frac{\partial \varphi}{\partial y} - \frac{\partial}{\partial y}\left(\frac{q\varphi}{h}\right)\right\} - \beta\frac{\varphi}{h}, \tag{A 5}$$

with the boundary conditions

$$q = 0 \quad (y = 0), \tag{A 6}$$

$$q = Fr(\varphi - \gamma h)^{\frac{1}{2}}h \quad (y = 1), \tag{A 7}$$

where τ has been replaced by t.

These equations are solved using the two-step Lax–Wendroff method described by Press *et al.* (1986, pp. 623–625) and Abbott & Basco (1989, pp. 225–234). This is an explicit finite-difference method that is accurate to second order in both time and space. Briefly, the scheme first uses the Lax method to integrate forward half a time step and estimate the variables on a staggered spatial grid that is offset by half a spatial step relative to the initial grid. The equations are then integrated a full time step forward, back onto the original grid, using a centred time and centred space integrating scheme with the points from the Lax method that are half a time step forward and the points at the current time step. Because the method is explicit, it requires only the current length and velocity at the nose of the gravity current, and not those values at the future time. Thus no iterations on the length and velocity at the nose are needed.

There are various advantages and disadvantages in using an explicit method rather than an implicit method for solving hyperbolic equations, and these are discussed at length in Abbott & Basco. We elected to use an explicit method because the computational algorithm does not depend upon if or where a shock exists. If it does exist, with the inherent or added numerical dissipation, the shock appears simply from the integration. This is unlike implicit schemes, for which several algorithms are necessary to handle the different regions of flow on either side of the shock. To know where to apply these algorithms, the shock velocity and strength must also be determined as part of the problem, which is an added complication. An explicit scheme has the disadvantage that a small time step is required to ensure numerical stability, but it only takes two or three minutes to run a simulation on a SUN IPC, so execution time is really not an issue. A difficulty with using explicit schemes for solving hyperbolic equations, which is minor compared with the advantage of using them for dealing with shocks, is that the points at the boundaries must be computed with an auxiliary method.

The evolution of the interior differencing points is completely specified by the Lax–Wendroff method, but this is not so for the end points. There are two boundary conditions specified, but six variables must be determined at the end points, so we need to specify four more conditions. We note that there can be no more additional boundary conditions; one at each end, as we shall see, is exactly the number that may be specified. The additional conditions are provided by the characteristic equations at each boundary.

There are three characteristic velocities in the flow, which are

$$\mathrm{d}y/\mathrm{d}t = c_{\pm} = x_{\mathrm{N}}^{-1}(u - y\dot{x}_{\mathrm{N}} \pm [(\phi-\gamma)h]^{\frac{1}{2}}), \tag{A 8}$$

$$\mathrm{d}y/\mathrm{d}t = c = x_{\mathrm{N}}^{-1}(u - y\dot{x}_{\mathrm{N}}) \tag{A 9}$$

in the transformed coordinate system, where (A 8) corresponds to the forward- and backward-propagating wave speed for shallow-water waves, and (A 9) is the rate that particles are advected in the flow. For a hyperbolic system of equations, the number and location of specified boundary conditions are the number and location of characteristics that propagate into the flow domain. By inspection of (A 8) and (A 9), there is one inward-propagating characteristic with velocity c_- at $y = 1$, since $u = \dot{x}_{\mathrm{N}}$ at $y = 1$, and another with velocity c_+ at $y = 0$. Thus the condition of no flow at $y = 0$ and the nose condition at $y = 1$ are indeed the most that we can specify.

The other conditions on the boundaries are determined from the characteristic equations that are satisfied along the characteristics that are not inwardly propagating. At $y = 0$ these are

$$\mathrm{d}\phi/\mathrm{d}t = -\beta\phi/h \quad \text{on} \quad \mathrm{d}y/\mathrm{d}t = 0, \tag{A 10}$$

$$\frac{\mathrm{d}}{\mathrm{d}t}\left(u - 2[(\phi-\gamma)h]^{\frac{1}{2}}\right) + \frac{1}{2}\left(\frac{h}{\phi}\right)^{\frac{1}{2}}\frac{\mathrm{d}\phi}{\mathrm{d}t} = 0 \quad \text{on} \quad \frac{\mathrm{d}y}{\mathrm{d}t} = x_{\mathrm{N}}^{-1}\left(u - y\dot{x}_{\mathrm{N}} - [(\phi-\gamma)h]^{\frac{1}{2}}\right), \tag{A 11}$$

$$u = 0 \quad \text{at} \quad y = 0, \tag{A 12}$$

and at $y = 1$ these are

$$\mathrm{d}\phi/\mathrm{d}t = -\beta\phi/h \quad \text{on} \quad \mathrm{d}y/\mathrm{d}t = 0, \tag{A 13}$$

$$\frac{\mathrm{d}}{\mathrm{d}t}\left(u + 2[(\phi-\gamma)h]^{\frac{1}{2}}\right) - \frac{1}{2}\left(\frac{h}{\phi}\right)^{\frac{1}{2}}\frac{\mathrm{d}\phi}{\mathrm{d}t} = 0 \quad \text{on} \quad \frac{\mathrm{d}y}{\mathrm{d}t} = x_{\mathrm{N}}^{-1}\left(u - y\dot{x}_{\mathrm{N}} + [(\phi-\gamma)h]^{\frac{1}{2}}\right), \tag{A 14}$$

$$u = Fr[(\phi-\gamma)h]^{\frac{1}{2}} \quad \text{at} \quad y = 1, \tag{A 15}$$

where we have reiterated the boundary conditions for completeness.

Here we obtain three equations and three unknowns at each boundary, and these are solved using the standard first-order method of characteristics. (Since the variables are only known at the grid points, spatial interpolation is used to determine their values on the appropriate characteristics that are projected towards the boundaries at the next time step.) The height, velocity and volume fraction of particles are then determined explicitly at each time step. Once the velocity at the front is known at the new time, the length of the gravity current is updated with a trapezoidal integrator, which is accurate to second order in time.

A.2. *Numerical dissipation*

The Lax–Wendroff scheme has an inherent numerical dissipation that damps high-frequency disturbances. This is sufficient for the resolution of weak shocks in hyperbolic systems, but to resolve strong shocks extra dissipation must be added to the momentum equations. Using a form suggested by Taylor (see Roache 1972, pp. 250–254), the momentum equation in (x, t)-coordinates becomes

$$\frac{\partial}{\partial t}(uh)+\frac{\partial}{\partial x}(uh^2+\tfrac{1}{2}(\phi-\gamma)h^2)=\frac{\partial}{\partial x}\left(\alpha_x\frac{\partial u}{\partial x}\right), \tag{A 16}$$

where

$$\alpha_x = b_1\Delta x(|u|+c_x)h, \tag{A 17}$$

and $c_x = u+[(\phi-\gamma)h]^{\frac{1}{2}}$ is the local wave speed. The parameter b_1 is some constant less than unity; a value of 0.3 was used for the simulations in this paper.

This added numerical dissipation has been shown to be very good at removing or at least minimizing high-frequency oscillations and overshoots that occur at shocks without changing the strength or velocity of the shock very much from the values one would derive analytically with jump conditions. The form of the dissipation is also constructed to be negligible except near the shock where the velocity (or height by virtue of the continuity equation) changes rapidly.

In the transformed space the momentum equation for the single-layer model with the extra numerical dissipation is

$$\frac{\partial q}{\partial t}=\frac{1}{x_{\mathrm{N}}}\left\{y\dot{x}_{\mathrm{N}}\frac{\partial q}{\partial y}-\frac{\partial}{\partial y}\left(\frac{q^2}{h}+\tfrac{1}{2}[(\varphi-\gamma)h]\right)\right\}+x_{\mathrm{N}}^{-1}\frac{\partial}{\partial y}\left\{\alpha_y\frac{\partial(q/h)}{\partial y}\right\}, \tag{A 18}$$

where

$$\alpha_y = b_1\Delta y(|u|+c_x)h. \tag{A 19}$$

The addition of the extra numerical dissipation does not change the size of the time steps or the stability of the method unless b_1 is too large. Because the extra dissipation is negligible everywhere except at the shocks, it need not be considered in determining the points on the boundaries with the method of characteristics as long as the shocks are not near these end points.

Appendix B. Critical Reynolds number

Initially, the dynamics of a gravity current of fixed volume are dominated by a balance between inertial and buoyancy forces. As the current lengthens and the velocity of its front decreases, however, viscous forces become increasingly important and eventually are more important than the inertial forces. The transition occurs when the ratio of the inertial forces to the viscous forces, the Reynolds number Re, is $O(1)$. The appropriate form of the Reynolds number for a gravity current and an estimate of its $O(1)$ value at the transition may be determined as follows.

Estimates of the inertial force F_i and the viscous force F_v in a gravity current are

$$F_i \approx \rho_c u_N^2 h_N w, \tag{B 1}$$

$$F_v \approx \mu x_N w u_N / h_N, \tag{B 2}$$

where w is the width of the current and μ is its viscosity. From the ratio of F_i to F_v, we find that the Reynolds number is defined by

$$Re = (u_N h_N / \nu)(h_N / x_N), \tag{B 3}$$

where ν is the kinematic viscosity of the gravity current, which is taken to be equal to that of the interstitial fluid in the particle-driven gravity current, consistent with the Boussinesq approximation used in §2. The critical value of the Reynolds number below which the current flows viscously is not known explicitly, but the experimental measurements have been made of the time for the transition from inertial to viscous flows for homogeneous gravity currents of fixed volume. From these results we may infer the critical value of the Reynolds number, Re_c.

For a homogeneous gravity current of fixed volume, the time t_c for the transition from an inertial current to a viscous current can be estimated from its similarity solution in the inertial regime. We recall from §2 that for such a current the dimensional length, velocity and height at the front of the current as functions of time are

$$x_N = C(g'q)^{\frac{1}{3}} t^{\frac{2}{3}}, \tag{B 4}$$

$$u_N = \tfrac{2}{3} C(g'q)^{\frac{1}{3}} t^{-\frac{1}{3}}, \tag{B 5}$$

$$h_N = q\lambda C^{-1}(g'q)^{-\frac{1}{3}} t^{-\frac{2}{3}}, \tag{B 6}$$

where C and λ are dimensionless constants that depend on the value of the Froude number used for the nose condition. If we insert these functions into the expression for the Reynolds number, we find Re_c as a function of t_c:

$$Re_c = \tfrac{2}{3}(\lambda/C)^2 (q^4/\nu^3 g'^2)^{\frac{1}{3}} t_c^{\frac{7}{3}}, \tag{B 7}$$

or, conversely, the time of transition is

$$t_c = K(q^4/\nu^3 q'^2)^{\frac{1}{7}}, \tag{B 8}$$

where

$$K = (\tfrac{2}{3}\lambda^2 / C^2 Re_c)^{\frac{3}{7}}. \tag{B 9}$$

The time of transition in (B 8) was derived by Huppert & Simpson (1980), who showed experimentally that $K = 0.5$. If we assume that $Fr = 1.19$ at the front of the current, then $C = 1.60$ and $\lambda = 1.31$. We can then solve for the critical Reynolds number to find that

$$Re_c = 2.25. \tag{B 10}$$

When the Reynolds number falls below this value, the flow of the current is dominated by a viscous–buoyancy balance.

REFERENCES

ABBOTT, M. B. & BASCO, D. R. 1989 *Computational Fluid Dynamics*. Longman Scientific & Technical.

BENJAMIN, T. B. 1968 Gravity currents and related phenomena. *J. Fluid Mech.* **88**, 223–240.

BONNECAZE, R. T., HUPPERT, H. E. & LISTER, J. R. 1993 Axisymmetric particle-driven gravity currents. *J. Fluid Mech.* (to be submitted).

CHEN, J. C. 1980 Studies on gravitational spreading currents. PhD thesis, California Institute of Technology.

EINSTEIN, H. A. 1968 Deposition of suspended particles in a gravel bed. *J. Hydraul. Div., ASCE* **94**, 1197–1205.

ELLISON, T. H. & TURNER, J. S. 1959 Turbulent entrainment in stratified flows. *J. Fluid Mech.* **6**, 423–447.

FANNELOP, T. K. & WALDMAN, G. D. 1972 Dynamics of oil slicks. *AIAA J.* **10**, 506–510.

GRUNDY, R. E. & ROTTMAN, J. W. 1986 Self-similar solutions of the shallow-water equations representing gravity currents with variable inflow. *J. Fluid Mech.* **169**, 337–351.

HALLWORTH, M. A., PHILLIPS, J., HUPPERT, H. E. & SPARKS, R. S. J. 1993 Entrainment in turbulent gravity currents. *Nature* (sub judice).

HOULT, D. P. 1972 Oil spreading on the sea. *Ann. Rev. Fluid Mech.* **4**, 341–368.

HUPPERT, H. E. 1982 The propagation of two-dimensional and axisymmetric viscous gravity currents over a rigid horizontal surface. *J. Fluid Mech.* **121**, 43–58.

HUPPERT, H. E. & SIMPSON, J. E. 1980 The slumping of gravity currents. *J. Fluid Mech.* **99**, 785–799.

INMAN, D. L., NORDSTROM, C. E. & FLICK, R. E. 1976 Currents in submarine canyons: an air–sea–land interaction. *Ann. Rev. Fluid Mech.* **8**, 275–310.

KÁRMÁN, T. VON 1940 The engineer grapples with nonlinear problems. *Bull. Am. Math. Soc.* **46**, 615–683.

MARTIN, D. & NOKES, R. 1988 Crystal settling in a vigorously convecting magma chamber. *Nature* **332**, 534–536.

MARTIN, D. & NOKES, R. 1989 A fluid-dynamical study of crystal settling in convecting magmas. *J. Petrol.* **30**, 1471–1500.

MCCAVE, I. N. 1970 Deposition of fine grained suspended sediment from tidal currents. *J. Geophys. Res.* **75**, 4151–4159.

PARKER, G., FUKUSHIMA, T. & PANTIN, H. M. 1986 Self-accelerating turbidity currents. *J. Fluid Mech.* **171**, 145–181.

PERRODON, A. 1985 Dynamics of oil and gas accumulation. *Bulletin des Centres de Recherches Exploration-Production, Elf-Aquitaine, Pau, France*, pp. 98–105.

PRESS, W. H., FLANNERY, B. P., TEUKLOSKY, S. A. & VETTERLING, W. T. 1986 *Numerical Recipes.* Cambridge University Press.

ROACHE, P. J. 1972 *Computational Fluid Dynamics.* Hermosa.

ROTTMAN, J. W. & SIMPSON, J. E. 1983 The initial development of gravity currents from fixed-volume releases of heavy fluids. *J. Fluid Mech.* **135**, 95–110.

SPARKS, R. S. J., BONNECAZE, R. T., HUPPERT, H. E., LISTER, J. R., HALLWORTH, M. A., MADER, H. & PHILLIPS, J. 1993 Sediment-laden gravity currents with reversing buoyancy. *Earth Planet. Sci. Lett.* **114**, 243–257.

WRIGHT, L. D., WISEMAN, W. J., YANG, Z. S., BORNHOLD, B. D., KELLER, G. H., PRIOR, D. B. & SUHAYDA, J. N. 1990 Processes of marine dispersal and deposition of suspended silts off the modern mouth of the Juanghe (Yellow River). *Contntl Shelf Res.* **10**, 1–40.